EDGE ARTICLE
Yu Wang *et al.*
In situ modification of the d-band in the core–shell structure
for efficient hydrogen storage *via* electrocatalytic N₂ fixation

EDGE ARTICLE

Check for updates

In situ modification of the d-band in the core–shell structure for efficient hydrogen storage *via* electrocatalytic N₂ fixation†

Xiaohui Yang,‡[ab] Jin Wan,‡[a] Huijuan Zhang[a] and Yu Wang 🄳 *[ac]

The electrochemical N₂ reduction reaction (NRR) into NH₃, especially powered by clean and renewable electricity, is a promising alternative to the capital- and energy-intensive Haber–Bosch process. However, the inert N≡N bond and the frantic competition of the hydrogen evolution reaction lead to a poor NH₃ yield rate and faradaic efficiency (FE). Here, we *in situ* construct a series of two-dimension core/shell V_2O_3/VN nanomeshes with a gradient nitride-layer thickness. Among them, V_2O_3/VN-2 exhibits the highest FE of 34.9%, an excellent NH₃ yield rate of 59.7 $\mu g\ h^{-1}\ mg_{cat.}^{-1}$, and outstanding cycle stability, exceeding those of most of the NRR electrocatalysts reported to date. First-principles calculations reveal that the d-band center of VN shifts up in a nearly linear manner with the decrease of nitride-layer thickness, and V_2O_3/VN-2 with a d-band center closer to the Fermi level can strengthen the d–2π* coupling between the catalyst and N₂ molecule, notably facilitating the N₂-into-NH₃ conversion.

Introduction

With the climate change due to the excessive use of fossil fuels, a low-carbon energy transition is permeating many industrialized countries, which stresses the importance of hydrogen energy in optimizing their energy structures.[1,2] Recently, ammonia (NH₃), as a medium of clean hydrogen energy storage, has attracted considerable attention due to its high energy density (4.32 kW h L⁻¹), low pressure storage, and convenient transport.[3,4] Compared with the capital- and energy-intensive Haber–Bosch process, the electrochemical N₂ reduction reaction (NRR) under ambient conditions is emerging as a promising alternative for the sustainable synthesis of NH₃.[5–8] Due to the high ionization energy (15.58 eV) of inert N₂ and the sluggish reaction kinetics involving six proton-coupled electron transfer steps, an electrocatalyst is requisite in N₂ adsorption and activation during the NRR process.[9–11] Although tremendous efforts have been devoted to the screening and development of new electrocatalysts and optimizing the electronic

aSchool of Chemistry and Chemical Engineering, State Key Laboratory of Power Transmission Equipment & System Security and New Technology, Chongqing University, 174 Shazheng Street, Shapingba District, Chongqing City, 400044, P. R. China. E-mail: wangy@cqu.edu.cn

bKey Laboratory of Reservoir Aquatic Environment, Chongqing Institute of Green and Intelligent Technology, Chinese Academy of Sciences, No. 266, Fangzheng Avenue, Beibei District, Chongqing 400714, P. R. China

cSchool of Electrical Engineering, Chongqing University, 174 Shazheng Street, Shapingba District, Chongqing City, 400044, P. R. China

† Electronic supplementary information (ESI) available. See https://doi.org/10.1039/d2sc03975c

‡ These authors contributed equally to this work.

structure, including noble-metal-based materials,[12,13] metal-oxide materials,[14,15] and metal-free materials,[16,17] their NRR efficiency is still very poor and far from meeting the needs of practical industrial production.[18] Thus, designing and fabricating potential electrocatalysts with high activity and selectivity is urgent and significant for the development of sustainable electrochemical NRR technology.

Transition metal nitrides (TMNs) are considered to be one of the best promising NRR candidates because their inherent feature endows them with unique advantages in electrochemically reducing N₂ into NH₃ along with the more favorable Mars–van Krevelen (MvK) pathway.[19–24] Several recent studies suggest that introducing dopants and/or defects into TMNs has also been proved to be an effective means to improve their electrocatalytic NRR performance compared with their counterparts.[25–27] The interesting thing is that introducing an O atom onto the VN surface is beneficial for the activation of the surface N sites adjacent to the surface O, where the introduction of O can regulate the electronic structure of nitride and weaken the V–N bond energy, which lowers the energy barrier of NH₃ release and thus facilitates the NRR progress.[28] In this regard, it is possible to modify the TMN electron state using the relevant oxide to achieve high NRR performance.

Shifting the d-band position up or down in the active site of the electrocatalyst may be an effective strategy to tune the TMN electron state to achieve the desired catalytic performance.[29,30] For instance, experimentally, Ling *et al.* reported that using the zeolitic-imidazole framework lowered the d-band position of Au/Pt to weaken H adsorption and concurrently constructed abundant electron-deficient sites to kinetically boost the NRR performance.[31] Huang *et al.* developed a class of M–Te (M = Ru,

Rh, Ir) glassy porous nanorods with a higher d-band center, showing better NRR activity.[32] Unfortunately, regulating the d-band state close to the Fermi level to enhance the interaction of N_2 with the substrate also leads to strong metal-H formation. Inspired by the above reports, how to develop a novel strategy by modifying the d-band center for improving NRR activity and simultaneously suppressing the competitive hydrogen evolution reaction (HER) will be an interesting topic.

In this work, we report the effect of d-band modification on NRR performance by engineering the core–shell nanostructure (CSN) consisting of an oxide core and a nitride shell, where d-band regulation is realized by controlling the thickness of the nitride shell *in situ* grown on the oxide core. Considering the influential role of vanadium (V) in nitrogenases,[33] hypotoxicity of V_2O_3,[34,35] and inactiveness of vanadium nitride (VN) for the HER,[19,22] we take core/shell V_2O_3/VN as a proof-of-concept platform. Interestingly, the NRR catalytic results show that as the nitride-layer thickness increases, the NH_3 yield of core/shell V_2O_3/VN first increases and then decreases, with the highest faradaic efficiency (FE) being 34.9% along with an excellent NH_3 yield rate of 59.7 μg h^{-1} mg$_{cat.}^{-1}$, significantly better than most literature reports. Furthermore, density functional theory (DFT) calculations demonstrate a similar phenomenon that when the thickness of the nitride shell is 2 atomic-layer, the barrier of the potential-determining step (PDS) for the NRR is minimum, only 0.63 eV. These results suggest that the more appropriate the nitriding time, the better the NRR activity.

Results and discussion

It is widely accepted that a two-dimensional (2D) porous morphology of the catalyst could impart high catalytic activity due to the high active-site exposure and the favorable mass/charge transport. To this end, a 2D porous V_2O_3 nanomesh as the oxide core and an *in situ* grown nitride shell with controllable thickness are fabricated as shown in Fig. 1a (see ESI† for more details). Initially, the precursor of 2D $Zn_3(OH)_2(V_2O_7)(H_2O)_2$ nanosheets with a nanoscale thickness of ~50 nm was prepared based on our previous studies (Fig. S1†).[36] Then, this sheet-like precursor was annealed in an argon atmosphere to form 2D porous V_2O_3 nanomeshes (Fig. S2†). 2D porous core/shell V_2O_3/VN nanomeshes with a gradient thickness of the nitride shell were obtained *via* an appropriate nitriding treatment, where the target samples were defined as V_2O_3/VN-*X* (*X* = 0.5, 2, 10, representing the nitriding time). For comparison, 2D porous pure VN nanomeshes were also prepared by lengthening the time of nitriding treatment.

Fig. 1b shows the transmission electron microscopy (TEM) image of 2D core/shell V_2O_3/VN-2 nanomeshes. Compared with the pure V_2O_3 core, no obvious change is observed in the morphology. The magnified TEM image shows that the surface of V_2O_3/VN-2 is rough, suggesting that a nitride layer has been formed (Fig. 1c). In addition, V_2O_3/VN-2 exhibits a crystalline structure, as evidenced by the selected-area electron diffraction image (inset in Fig. 1c). Notably, the corresponding high-resolution TEM (HRTEM) image of V_2O_3/VN-2 exhibits well-defined lattice fringes, and a lattice plane distance of

0.247 nm along different directions, which was indexed to the (110) or (1$\bar{2}$0) facet of the rhombohedral V_2O_3 phase (PDF #71-0280). In contrast, the thickness of the VN shell is about 0.5 nm, and the crystallinity is low which may be attributed to the short time of nitriding. Furthermore, a high-angle annular dark-field scanning transmission electron microscope (HAADF-STEM) equipped with an energy-dispersive spectrometer (EDS) was employed to investigate the compositional distribution of this 2D core/shell V_2O_3/VN-2 nanomesh. The V element is uniformly distributed over the whole nanomesh skeleton, while the O element is distributed in the core area and the amount of N is comparatively higher in the boundary region (Fig. 1e–h). We further investigated other as-synthesized samples with different nitriding treatments. From the HAADF-STEM images and corresponding compositional distributions (Fig. S3†), it can be seen that the nitriding process is from outside to inside with the increase of nitriding time, indicating that the length of nitriding time determines the thickness of the VN shell in 2D core/shell V_2O_3/VN nanomeshes. Moreover, the structure of the 2D porous nanomeshes remains unchanged even if the oxide core is subjected to different degrees of nitridation or even converted to pure VN, which implies excellent structural stability.

To further study the crystal phases of all 2D porous nanomesh samples, X-ray powder diffraction (XRD) analysis was carried out. As shown in Fig. 1i, all the diffraction peaks of the core are well indexed to rhombohedral V_2O_3, in agreement with the TEM results. As nitriding time increases, the intensity of V_2O_3 diffraction peaks gradually decreases while new peaks assigned to the cubic VN (PDF #65-4307) are detected. It is noted that the diffraction peaks of nitride shells in V_2O_3/VN-0.5 and V_2O_3/VN-2 are not obvious, which is mainly caused by the inherent strong penetrability of XRD. Therefore, we further employ X-ray photoelectron spectroscopy (XPS) to research their surface chemical states. The XPS full spectra of all 2D porous nanomesh samples are shown in Fig. S4,† from which the existence of V, O, and N elements except for the pure V_2O_3 sample is verified. Fig. 1j shows the high-resolution N 1s spectrum of V_2O_3/VN-2 that can be deconvoluted into four subpeaks. The two subpeaks at a lower binding energy (BE) of 397.3 and 396.5 eV are attributed to the bond of N–V and the N_xVO_y species, respectively.[37,38] The peak located at 401.4 eV is assigned to the residuals of ammonia/ammonium species adsorbed on the material surface during the nitriding treatment and the subpeak of 399.1 eV is considered a satellite peak.[28] In contrast, V_2O_3/VN-0.5 has only a satellite peak, indicating that N atoms dope in V_2O_3. The N 1s spectrum of deeper nitrided V_2O_3/VN-10 can also be deconvoluted into four subpeaks, where the intensity of the N–V bond increases while the N_xVO_y species decreases. According to the above analysis, it is found that the thickness of the VN shell varies with nitriding time.

Based on the above-mentioned characterization, a series of 2D porous core/shell V_2O_3/VN nanomeshes with a gradient thickness of the nitride shell have been successfully prepared. Next, their NRR performance was measured by evaluating their electrochemical N_2 reduction ability using a typical two-compartment cell separated by a proton exchange membrane.
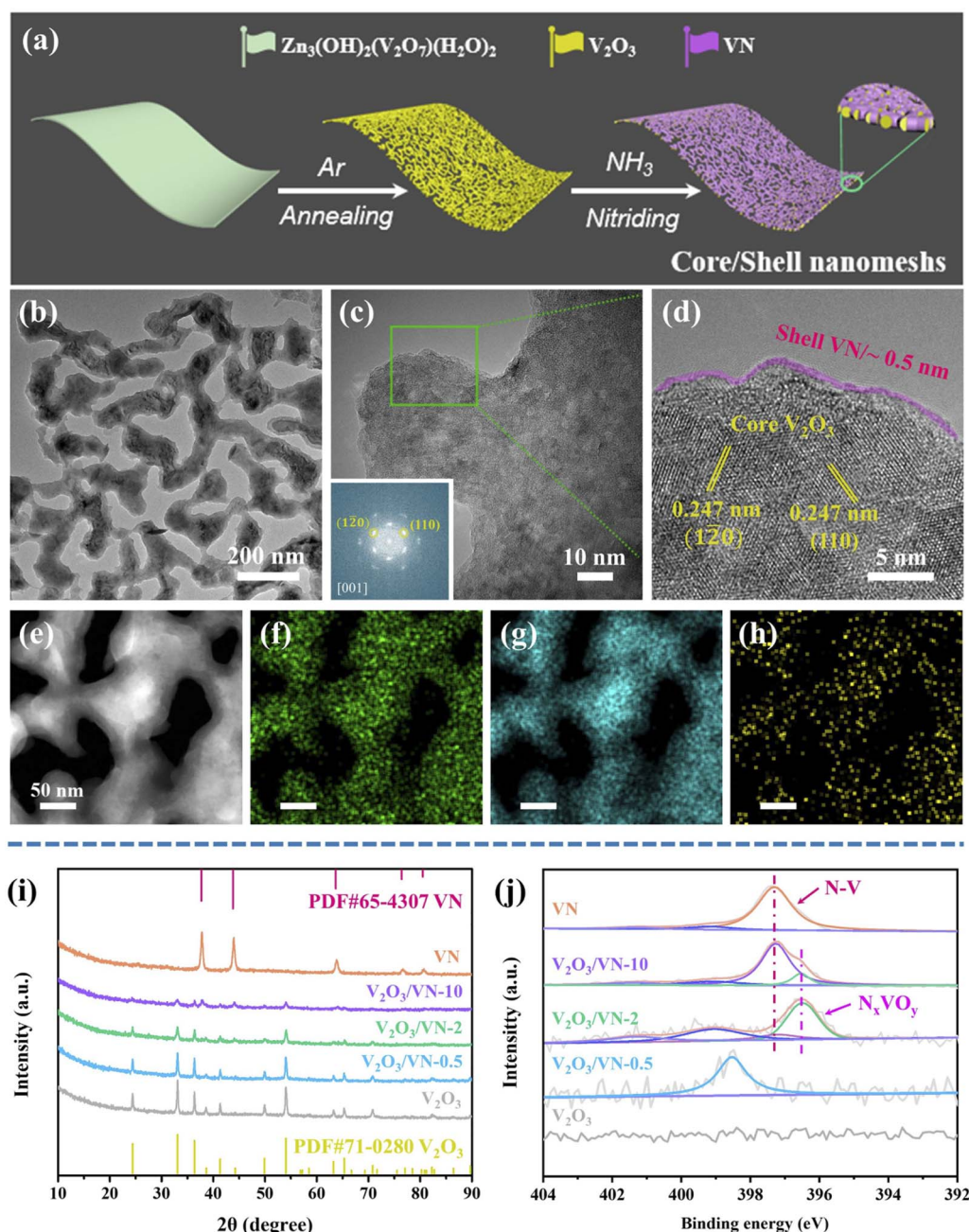
Fig. 1 (a) Schematic illustration of the fabrication of 2D core/shell V_2O_3/VN nanomeshes. Morphology and structure characterization for 2D core/shell V_2O_3/VN-2. (b) TEM image, (c) magnified TEM image, and (d) the corresponding HR-TEM image in the edge. (e) HAADF-STEM image, and the corresponding EDS elemental mapping images of (f) V, (g) O, and (h) N based on image (d). (i) XRD patterns and (j) XPS spectra of N 1s for pure V_2O_3 nanomeshes, core/shell V_2O_3/VN-X and pure VN nanomeshes. Inset in (c) is the corresponding selected-area electron diffraction.

We first choose V_2O_3/VN-2 as the research object. Its linear sweep voltammetric (LSV) curves in Ar- and N_2-saturated 0.05 M H_2SO_4 solution are shown in Fig. 2a, where an obviously increased reduction current density is detected in the N_2-saturated acid solution, especially in the potential window between −0.1 V and −0.6 V *vs.* RHE, indicating an additional contribution from the conversion reaction of N_2 to NH_3 in this system. And then NH_3 yield rates and corresponding FEs for V_2O_3/VN-2 were assessed by combining the chronoamperometry tests (Fig. S7†) and the corresponding UV-vis absorption spectra

(Fig. S8†) at different applied potentials. As shown in Fig. 2b, the highest NH_3 yield is 59.7 μg h^{-1} mg$_{cat.}^{-1}$, which is achieved at a driving potential of −0.4 V *vs.* RHE, while the highest FE value of 34.9% is reached at −0.2 V *vs.* RHE. To the best of our knowledge, such outstanding NRR performance is comparable with those of the most advanced NRR electrocatalysts recently reported in 0.1 M acid electrolyte under room temperature and atmosphere pressure (Fig. 2c and Table S1†). Meanwhile, V_2O_3/VN-2 also possesses excellent selectivity for NH_3 formation, which is verified by no N_2H_4 being detected (Fig. S9†). To

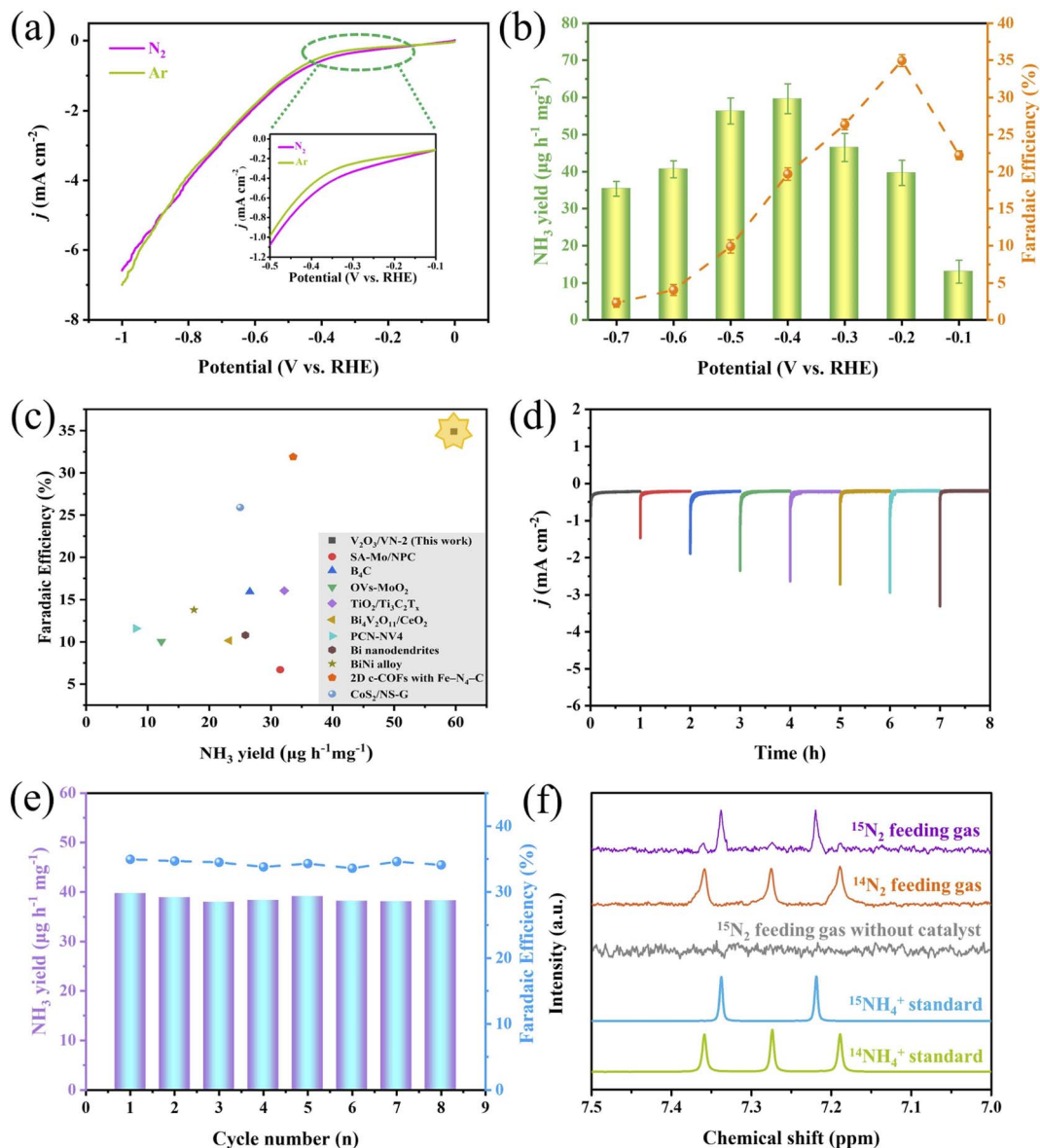**Fig. 2** Electrocatalytic NRR performance of 2D core/shell V_2O_3/VN-2 nanomeshes. (a) Linear sweep voltammetric curves in Ar- and N_2-saturated 0.05 M H_2SO_4 solution. Inset is the amplified details. (b) The average NH_3 yields and faradaic efficiencies (FEs) at different applied potentials. (c) Comparison of NH_3 yields and FEs with the recently well-developed NRR electrocatalysts in 0.1 M acid solution under room temperature and atmosphere pressure. (d) Cycling stability tests in N_2-saturated 0.05 M H_2SO_4 solution at a potential of -0.2 V vs. RHE under consecutive recycling electrolysis. (e) The corresponding NH_3 yields and FEs based on eight consecutive cycling tests. (f) ^1H NMR spectra of the concentrated electrolyte fed with $^{15}N_2$ and $^{14}N_2$ after the electrolytic reaction.

investigate the stability of V_2O_3/VN-2, consecutive cycling tests and long-term electrocatalytic tests were further carried out at -0.2 V vs. RHE. After eight consecutive cycling tests, there is no significant change in current densities, NH_3 yields and FEs (Fig. 2d and e). After a long-term electrocatalytic test for 50 h, the activity of V_2O_3/VN-2 nanomeshes remains unchanged with an NH_3 yield of 38.5 µg h^{-1} mg$_{cat.}^{-1}$ and FE of 35.6% (Fig. S10†). In addition, the SEM, TEM, and XRD results show that V_2O_3/VN-2 maintains its original morphology and crystal structure after electrocatalysis (Fig. S11 and S12†). All these results suggest that V_2O_3/VN-2 is a considerably robust NRR electrocatalyst.

To confirm the safety of the test environment, we conducted blank experiments with the fresh 0.05 M H_2SO_4 solution and the cycled 0.05 M H_2SO_4 electrolyte treated by N_2 gas bubbling for 1 h. No NH_3 was detected in both of them, which is verified by UV-vis spectroscopy (Fig. S13†), indicating that the test environment is secure. And then, a series of control experiments using a bare carbon paper electrode (CPE) in N_2-saturated electrolyte and a 2D core/shell V_2O_3/VN-2 nanomesh electrode in Ar/N_2-saturated electrolyte were performed to examine the source of the produced NH_3. The corresponding UV-vis absorption spectra are shown in Fig. S14.† Reasonably,
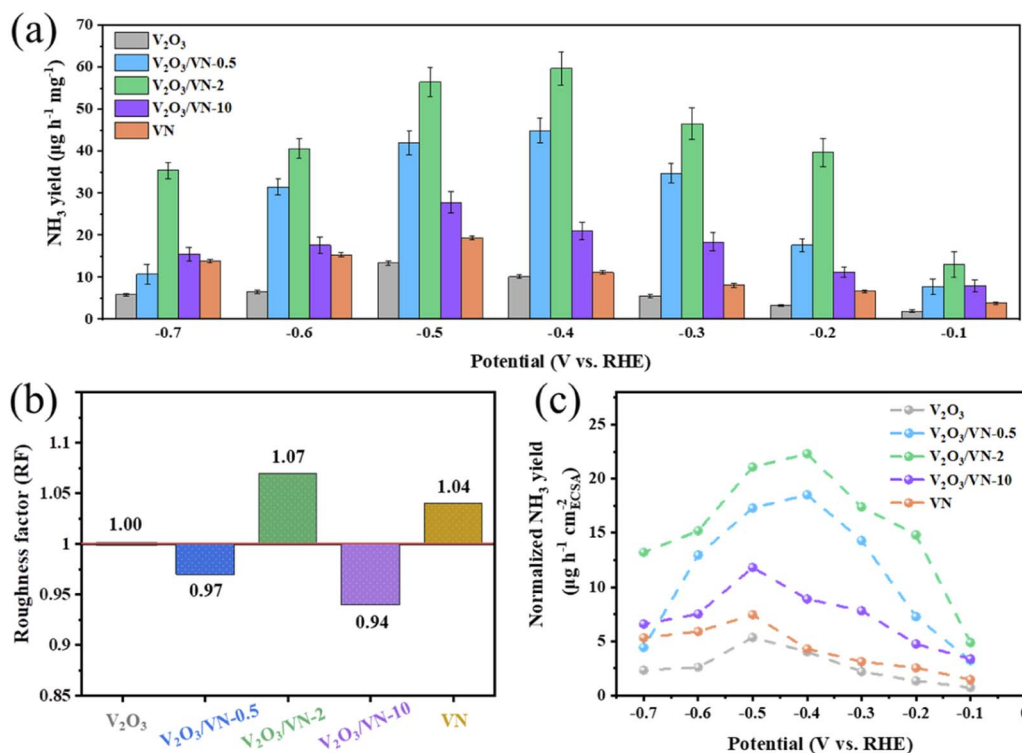
Fig. 3 (a) Comparison of the NH_3 yields for the pure V_2O_3 nanomeshes, core/shell V_2O_3/VN-X and pure VN nanomeshes in N_2-saturated 0.05 M H_2SO_4 solution at different applied potentials. (b) The roughness factors of core/shell V_2O_3/VN-X and pure VN nanomeshes taken with pure V_2O_3 nanomeshes as a reference. (c) ECSA-normalized NH_3 yields of all 2D porous nanomesh samples at each given potential.

a stronger signal for the core/shell V_2O_3/VN-2 electrode in N_2-saturated electrolyte is observed compared with the other two control experiments, which indicates that the NH_3 produced is derived from the electrochemical reduction of N_2 to NH_3 in the presence of the 2D core/shell V_2O_3/VN-2 catalyst. Furthermore, isotopic labeling experiments using $^{15}N_2$ and $^{14}N_2$ as feeding gases were carried out to identify the N source of the produced NH_3 and to probe into the potential pathway of V_2O_3/VN-2 during the NRR process. The characteristic signal, a doublet coupling for $^{15}NH_4^+$ and a triplet coupling for $^{14}NH_4^+$ in the ^1H nuclear magnetic resonance (^1H NMR) spectra, is used as a criterion of judgment. As shown in Fig. 2f, when $^{14}N_2$ as feeding gas is supplied, only triplet coupling from $^{14}NH_4^+$ was observed, and when $^{15}N_2$ as feeding gas is supplied, primary doublet coupling from $^{15}NH_4^+$ along with weak triplet coupling from $^{14}NH_4^+$ is detected. Such results suggest that 2D core/shell V_2O_3/VN-2 nanomeshes as an active catalyst can effectively catalyze the conversion of N_2 to NH_3. Besides, it is reasonably inferred that the surface N atom in 2D core/shell V_2O_3/VN-2 nanomeshes is first reduced to NH_3 and the rest of the N vacancies facilitate the continuous proceeding of the NRR, in line with the reported MvK pathway.

To attest the superiority of 2D core/shell V_2O_3/VN-2 nanomeshes, the NRR activities of all comparative samples were tested at different applied potentials, including pure V_2O_3 nanomeshes, core/shell V_2O_3/VN-0.5 nanomeshes, core/shell V_2O_3/VN-10 nanomeshes, and pure VN nanomeshes. Based on the results of UV-vis absorption spectra (Fig. S15†), their

respective NH_3 yields are obtained and shown in Fig. 3a. It is obvious that as the thickness of the nitride shell in all 2D porous nanomesh samples increases, the corresponding NH_3 yield first increases and then decreases at each given potential, where the sample of V_2O_3/VN-2 possesses the highest NRR activity. Furthermore, the electrochemically active surface area (ECSA) of each sample was obtained by evaluating their double-layer capacitance (C_{dl}) (Fig. S16 and S17†). To achieve the intrinsic activity (surface area normalized), here we introduce the concept of roughness factors (RFs) based on previous reports.[39–41] The RF value of pure V_2O_3 nanomeshes is supposed to be 1, RFs of the other samples were calculated by dividing their capacitances by the C_{dl} value of pure V_2O_3 nanomeshes (Fig. 3b). As shown in Fig. 3c, the ECSA-normalized NH_3 yields at different given potentials still first increase and then decrease with the growth of the nitride shell for all 2D porous nanomesh samples, indicating that only the sample with the appropriate thickness of the nitride shell has the best intrinsic NRR activity.

To further decode the origin of the improved NRR performance of 2D core/shell V_2O_3/VN nanomeshes, DFT calculations were performed to understand the response mechanism of reducing N_2 into NH_3 on these systems. The VN shell thickness observed in the HR-TEM image (~0.5 nm, Fig. 1d) suggests that the VN covering the (001) surface of V_2O_3 is almost two atomic-layer thick. Furthermore, the amount of nitriding time will lead to different thicknesses of the VN shell. According to these characterization results, four systems were constructed, including V_2O_3/N-doped, V_2O_3/VN-2 layer, V_2O_3/VN-3 layer, and

the (111) surface of pure VN, corresponding to V_2O_3/VN-X ($X =$ 0.5, 2, 10) and pure VN (Fig. S18†).

As we discussed above, this reaction will follow the MvK mechanism (Fig. S19–S22†). In the reaction procedure, the pre-reacted *N can be hydrogenated into the *NH intermediate via the proton/electron (H^+/e^-) pair. Then, the adsorbed *NH captures the H^+/e^- pair, forming the *NH_2. Subsequently, the *NH_2 is further hydrogenated to form N defects, while releasing the NH_3 molecule. Finally, the defect captures the N_2 molecule which is stepwise hydrogenated into *NNH, *NNH_2, and *NNH_3 until the second NH_3 molecule is released. Notably, the adsorption of N_2 is the potential-limiting step (PDS) for the

V_2O_3/VN-2 layer and V_2O_3/VN-3 layer with the maximum energy barrier of 0.63 and 0.70 eV, respectively. The V_2O_3/N-doped exhibits the largest reaction barrier of 0.88 eV when the first NH_3 is released. In addition, the free energy change of the *N_2 to *NNH step on V_2O_3/N-doped and pure VN surface is 0.83 and 0.80 eV, respectively (Fig. 4a). Thus, the calculated NRR performance on these systems follows the order of V_2O_3/VN-2 layer > V_2O_3/VN-3 layer > pure VN > V_2O_3/N-doped, which is highly consistent with the experimental results. In addition to the high NRR activity, an ideal catalyst should be able to suppress the HER to achieve high FE. Basically, if the adsorption free energy of the H adsorbate (ΔG_{*H}) is more negative than
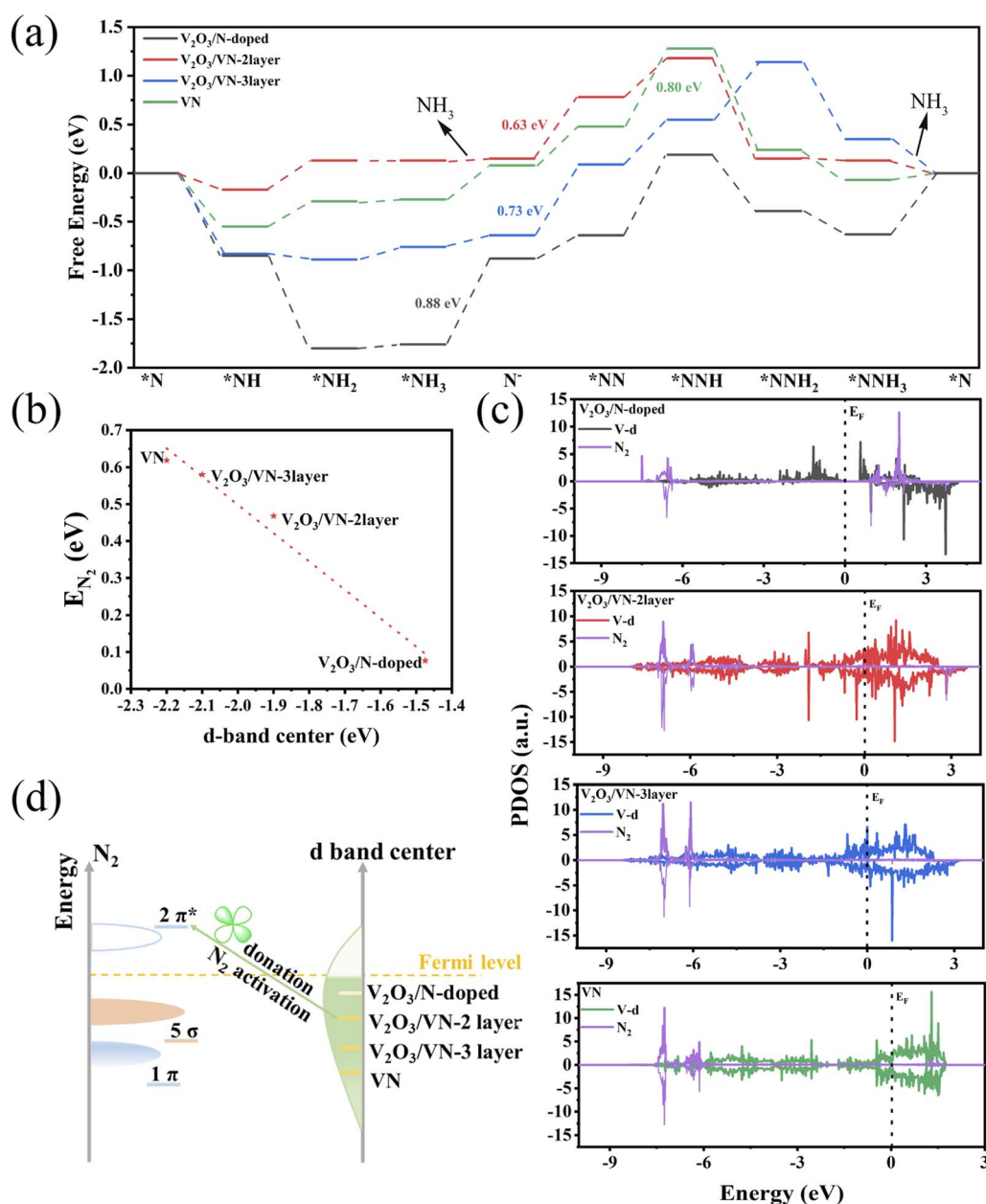

Fig. 4 (a) Gibbs free energy diagrams for N_2 electroreduction. (b) The linear relationship between the adsorption energy of N_2 and the d-band center on these four systems. (c) The PDOS of N_2 and the V d-band of N_2@V_2O_3/N-doped, N_2@V_2O_3/VN-2 layer, N_2@V_2O_3/VN-3 layer, and pure N_2@VN, respectively. (d) Schematic illustration explaining N_2 activation by altering the d-band center.

that for $*N_2$, $*H$ can easily cover the active sites and block the NRR. As shown in Fig. S23,† V_2O_3/VN-2 layer presents the highest ΔG_{*H}, which is much larger than the $*N_2$ adsorption energy, indicating that d-band modification can effectively promote NRR actively while suppressing the competitive HER.

The electrocatalytic performance is closely related to the valence electron of the active sites. The d-band center is often used as a descriptor to predict and describe the interaction between the catalyst and the adsorbate. Inspired by previous work,[42] the higher d-band center of the metal indicates a stronger interaction with the adsorbate state, which is beneficial for NRR performance. As shown in Fig. S24,† as the nitriding time increases, the d-band center of the active sites gradually shifted away from the Fermi level, indicating weakened binding strength. Except for the V_2O_3/N-doped, the d-band of the other three systems across the Fermi level exhibits a metallic character. Although the V_2O_3/N-doped exhibits the highest d-band center, there is a significant gap between the valence band and the conduction band, which limits charge transfer and electro-catalytic kinetics. Furthermore, the adsorption energy of N_2 on these four systems decreases in a nearly linear manner with the downshifts of the d-band center (Fig. 4b).

The $*N_2$ to $*NNH$ step is widely considered to be the PDS due to the inert $N\equiv N$ bond.[43,44] To understand the underlying mechanism of the N_2 activation, we investigated the partial density of states (PDOS) for free N_2 and N_2 adsorbed on these four systems with N vacancies. As shown in Fig. S25,† the occupied 1π and 5σ molecular orbitals of free N_2 are located below the Fermi level, and can donate electrons to the unoc-cupied d orbitals of the systems, forming bonding states. Moreover, the unoccupied $2\pi^*$ orbitals of N_2 accept electrons from occupied d orbitals of the metal, leading to the partially occupied $2\pi^*$ orbitals downshifting to the Fermi level. The "donation–back donation" between the metal and adsorbate can activate the adsorbed N_2 (Fig. 4c). To be specific, for V_2O_3/VN-2 layer, V_2O_3/VN-3 layer, and pure VN, after adsorption of the free N_2 on N defects, the antibonding $2\pi^*$ orbitals of N_2 strongly hybridize with the occupied d orbitals of active site V, especially for V_2O_3/VN-2 layer, indicating that more effective N_2 activation occurs in V_2O_3/VN-2 layer. The results are in accord with the d-band center values for different core/shell V_2O_3/VN samples. Benefiting from the upper d-band of V_2O_3/VN-2 layer and thus closer energy level difference with unoccupied $2\pi^*$ orbitals of N_2, the π bond was constructed through side-to-side overlap of V-d orbitals and $2\pi^*$ orbitals of N_2 according to the molecular orbital theory. Thus, the effective electron conductive channel is built in V_2O_3/VN-2 layer through the V–N π bond; in other words, the electron transfer from partially occupied d-orbitals to the $2\pi^*$ antibonding orbitals can easily occur in the catalytic process. In contrast, although the 1π and 5σ orbitals of N_2 interact strongly with the d orbital of V_2O_3/N-doped, the anti-bonding orbitals $2\pi^*$ of N_2 are still located above the Fermi level and fail to activate the nitrogen. Furthermore, this strong interaction also leads to difficulties in the desorption of NH_3. Consequently, suitable nitriding of V_3O_2 can balance the d-band center and electron conduction of the surface V, leading to outstanding NRR performance (Fig. 4d).

Conclusions

In summary, we have successfully constructed a stable NRR catalytic active intermediate of N_xVO_y species in 2D core/shell V_2O_3/VN nanomeshes and demonstrated that d-band modifica-tion is the key to enhance the NRR performance. Surprisingly, when employed in the electrochemical reduction of N_2 to NH_3, this 2D core/shell V_2O_3/VN-2 nanomesh achieves the highest FE of 34.9% among all recently reported advanced NRR electrocatalysts in an acid electrolyte under ambient conditions. Moreover, this catalyst also exhibits an excellent NH_3 yield of 59.7 µg h^{-1} mg$_{cat.}^{-1}$ and outstanding stability without significant loss of activity after eight consecutive cycling tests and a long-term electrocatalytic test for 50 h. Isotopic labeling experiments combined with ^1H NMR spectroscopy further confirm the reaction mechanism following the MvK pathway during the NRR process. DFT calculations reveal that the V_2O_3 core can tune the d-band structure of the VN shell, strengthen the interaction between N_2 and the active site, and thus reduce the NRR potential barrier toward significantly enhanced electrochemical NRR performance. This study not only opens up a new avenue to develop high-efficiency NRR catalysts, but also guides to design other advanced catalysts for challenging electrocatalytic reactions for renewable energy conversion.

Data availability

The data that support the findings of this study are available from the corresponding authors upon reasonable request.

Author contributions

Y. W. and X. H. Y. developed the research concept, X. H. Y. prepared the materials, performed the electrochemical experi-ments, and analyzed the data. J. W. provided the theoretical calculations. X. H. Y. and J. W. contributed to the interpretation of the results and the writing of the manuscript, which was revised by H. J. Z. All authors contributed to the scientific discussions.

Conflicts of interest

The authors declare no conflict of interest.

Acknowledgements

References

1 L. Pingkuo and H. Xue, *Int. J. Hydrog. Energy*, 2022, **47**, 9485–9503.

2 X. Peng, H. X. Liu, Y. Zhang, Z. Q. Huang, L. Yang, Y. Jiang, X. Wang, L. Zheng, C. Chang, C. T. Au, L. Jiang and J. Li, *Chem. Sci.*, 2021, **12**, 7125–7137.

3 Y. Abghoui and E. Skulason, *Catal. Today*, 2017, **286**, 69–77.

4 L. Li, C. Tang, H. Jin, K. Davey and S.-Z. Qiao, *Chem*, 2021, **7**, 3232–3255.

5 J. G. Chen, R. M. Crooks, L. C. Seefeldt, K. L. Bren, R. M. Bullock, M. Y. Darensbourg, P. L. Holland, B. Hoffman, M. J. Janik, A. K. Jones, M. G. Kanatzidis, P. King, K. M. Lancaster, S. V. Lymar, P. Pfromm, W. F. Schneider and R. R. Schrock, *Science*, 2018, **360**, eaar6611.

6 Z. W. Seh, J. Kibsgaard, C. F. Dickens, I. B. Chorkendorff, J. K. Norskov and T. F. Jaramillo, *Science*, 2017, **355**, eaad4998.

7 G. Soloveichik, *Nat. Catal.*, 2019, **2**, 377–380.

8 J. Wan, Y. Wang, W. Tian, H. Zhang and Y. Wang, *Appl. Surf. Sci.*, 2021, **569**, 151020.

9 A. R. Singh, B. A. Rohr, J. A. Schwalbe, M. Cargnello, K. Chan, T. F. Jaramillo, I. Chorkendorff and J. K. Norskov, *ACS Catal.*, 2017, **7**, 706–709.

10 X. Guo, J. Gu, S. Lin, S. Zhang, Z. Chen and S. Huang, *J. Am. Chem. Soc.*, 2020, **142**, 5709–5721.

11 D. Yao, C. Tang, L. Li, B. Xia, A. Vasileff, H. Jin, Y. Zhang and S. Z. Qiao, *Adv. Energy Mater.*, 2020, **10**, 2001289.

12 H. Huang, L. Xia, X. Shi, A. M. Asiri and X. Sun, *Chem. Commun.*, 2018, **54**, 11427–11430.

13 W. Cai, Y. Han, Y. Pan, X. Zhang, J. Xu, Y. Zhang, Y. Sun, S. Li, J. Lai and L. Wang, *J. Mater. Chem. A*, 2021, **9**, 13483–13489.

14 T. Wu, H. Zhao, X. Zhu, Z. Xing, Q. Liu, T. Liu, S. Gao, S. Lu, G. Chen, A. M. Asiri, Y. Zhang and X. Sun, *Adv. Mater.*, 2020, **32**, e2000299.

15 K. Chu, Q. Q. Li, Y. H. Cheng and Y. P. Liu, *ACS Appl. Mater. Interfaces*, 2020, **12**, 11789–11796.

16 S. Zhao, X. Lu, L. Wang, J. Gale and R. Amal, *Adv. Mater.*, 2019, **31**, e1805367.

17 Y. Yang, L. Zhang, Z. Hu, Y. Zheng, C. Tang, P. Chen, R. Wang, K. Qiu, J. Mao, T. Ling and S. Z. Qiao, *Angew. Chem., Int. Ed.*, 2020, **59**, 4525–4531.

18 D. Yao, C. Tang, P. Wang, H. Cheng, H. Jin, L.-X. Ding and S.-Z. Qiao, *Chem. Eng. Sci.*, 2022, **257**, 117735.

19 Y. Abghoui and E. Skúlason, *Catal. Today*, 2017, **286**, 78–84.

20 R. Zhang, Y. Zhang, X. Ren, G. Cui, A. M. Asiri, B. Zheng and X. Sun, *ACS Sustain. Chem. Eng.*, 2018, **6**, 9545–9549.

21 L. Zhang, X. Ji, X. Ren, Y. Luo, X. Shi, A. M. Asiri, B. Zheng and X. Sun, *ACS Sustain. Chem. Eng.*, 2018, **6**, 9550–9554.

22 Y. Abghoui, A. L. Garden, J. G. Howalt, T. Vegge and E. Skúlason, *ACS Catal.*, 2016, **6**, 635–646.

23 X. Yang, S. Kattel, J. Nash, X. Chang, J. H. Lee, Y. Yan, J. G. Chen and B. Xu, *Angew. Chem., Int. Ed.*, 2019, **58**, 13768–13772.

24 J. Nash, X. Yang, J. Anibal, M. Dunwell, S. Yao, K. Attenkofer, J. G. Chen, Y. Yan and B. Xu, *J. Phys. Chem. C*, 2019, **123**, 23967–23975.

25 X. Yang, F. Ling, J. Su, X. Zi, H. Zhang, H. Zhang, J. Li, M. Zhou and Y. Wang, *Appl. Catal., B*, 2020, **264**, 118477.

26 H. Jin, L. Li, X. Liu, C. Tang, W. Xu, S. Chen, L. Song, Y. Zheng and S. Z. Qiao, *Adv. Mater.*, 2019, **31**, 1902709.

27 Q. Li, L. He, C. Sun and X. Zhang, *J. Phys. Chem. C*, 2017, **121**, 27563–27568.

28 X. Yang, J. Nash, J. Anibal, M. Dunwell, S. Kattel, E. Stavitski, K. Attenkofer, J. G. Chen, Y. Yan and B. Xu, *J. Am. Chem. Soc.*, 2018, **140**, 13387–13391.

29 H. Y. F. Sim, J. R. T. Chen, C. S. L. Koh, H. K. Lee, X. Han, G. C. Phan-Quang, J. Y. Pang, C. L. Lay, S. Pedireddy, I. Y. Phang, E. K. L. Yeow and X. Y. Ling, *Angew. Chem., Int. Ed.*, 2020, **59**, 16997–17003.

30 J. Wang, B. Huang, Y. Ji, M. Sun, T. Wu, R. Yin, X. Zhu, Y. Li, Q. Shao and X. Huang, *Adv. Mater.*, 2020, **32**, e1907112.

31 H. Y. F. Sim, J. R. T. Chen, C. S. L. Koh, H. K. Lee, X. Han, G. C. Phan-Quang, J. Y. Pang, C. L. Lay, S. Pedireddy, I. Y. Phang, E. K. L. Yeow and X. Y. Ling, *Angew. Chem., Int. Ed.*, 2020, **59**, 16997–17003.

32 J. Wang, B. Huang, Y. Ji, M. Sun, T. Wu, R. Yin, X. Zhu, Y. Li, Q. Shao and X. Huang, *Adv. Mater.*, 2020, **32**, 1907112.

33 R. R. Eady, *Chem. Rev.*, 1996, **96**, 3013–3030.

34 N. Rajendran, J. C. Seagrave, L. M. Plunkett and J. A. MacGregor, *Inhalation Toxicol.*, 2016, **28**, 618–628.

35 R. Zhang, J. Han, B. Zheng, X. Shi, A. M. Asiri and X. Sun, *Inorg. Chem. Front.*, 2019, **6**, 391–395.

36 W. Fu, Y. Wang, H. Zhang, M. He, L. Fang, X. Yang, Z. Huang, J. Li, X. Gu and Y. Wang, *J. Catal.*, 2019, **369**, 47–53.

37 N. C. Saha and H. G. Tompkins, *J. Appl. Phys.*, 1992, **72**, 3072–3079.

38 A. Glaser, S. Surnev, F. P. Netzer, N. Fateh, G. A. Fontalvo and C. Mitterer, *Surf. Sci.*, 2007, **601**, 1153–1159.

39 L. Hu, A. Khaniya, J. Wang, G. Chen, W. E. Kaden and X. Feng, *ACS Catal.*, 2018, **8**, 9312–9319.

40 Y. Wang, M. M. Shi, D. Bao, F. L. Meng, Q. Zhang, Y. T. Zhou, K. H. Liu, Y. Zhang, J. Z. Wang, Z. W. Chen, D. P. Liu, Z. Jiang, M. Luo, L. Gu, Q. H. Zhang, X. Z. Cao, Y. Yao, M. H. Shao, Y. Zhang, X. B. Zhang, J. G. Chen, J. M. Yan and Q. Jiang, *Angew. Chem., Int. Ed.*, 2019, **58**, 9464–9469.

41 X. Yang, F. Ling, X. Zi, Y. Wang, H. Zhang, H. Zhang, M. Zhou, Z. Guo and Y. Wang, *Small*, 2020, **16**, 2000421.

42 J. K. Norskov, T. Bligaard, J. Rossmeisl and C. H. Christensen, *Nat. Chem.*, 2009, **1**, 37–46.

43 Y. Liao, J. Qian, G. Xie, Q. Han, W. Dang, Y. Wang, L. Lv, S. Zhao, L. Luo, W. Zhang, H.-Y. Jiang and J. Tang, *Appl. Catal., B*, 2020, **273**, 119054.

44 X. Yan, D. Liu, H. Cao, F. Hou, J. Liang and S. X. Dou, *Small Methods*, 2019, **3**, 1800501.